Research Square

Preprints are preliminary reports that have not undergone peer review.
They should not be considered conclusive, used to inform clinical practice,
or referenced by the media as validated information.

Synthesis, Characterization and In Vitro Biological Evaluation of Nickel-Doped Iron Oxide Nanoparticles for Antimicrobial, Antioxidant, and Anticancer Applications

Munazza Perveen
University of Okara
Ali Umar
University of Okara
Muhammad Khalil Ahmad Khan
University of Okara
Muhammad Khan
University of the Punjab
Muhammad Saleem Khan
University of Okara
Muhammad Wajid
University of Okara
Misbah Ullah Khan
misbahullahkhan143@uo.edu.pk
University of Okara

Research Article

Keywords: Nickel-doped iron oxide, Hematite, Nanoparticles, Co-precipitation, Antimicrobial, Antioxidant, Anticancer, MTT assay, Magnetic properties, Reactive oxygen species

Posted Date: November 25th, 2026

DOI: https://doi.org/10.21203/rs.3.rs-11758509/v1

License: This work is licensed under a Creative Commons Attribution 4.0 International License.
Read Full License

Additional Declarations: No competing interests reported.

Synthesis, Characterization and In Vitro Biological Evaluation of Nickel-Doped Iron Oxide Nanoparticles for Antimicrobial, Antioxidant, and Anticancer Applications

Munazza Perveen[1*], Ali Umar[1], Muhammad Khalil Ahmad Khan[1], Muhammad Khan[2], Muhammad Saleem Khan[1], Muhammad Wajid[1], Misbah Ullah Khan[3*]

[1]Department of Zoology, Faculty of Life Sciences, University of Okara, Okara 56130, Pakistan

[2]Institute of Zoology, University of the Punjab, Lahore 54590, Pakistan

[3]Center for Nanosciences, University of Okara, Okara 56130, Pakistan

Correspondence : M.U.K (misbahullahkhan143@uo.edu.pk)**;** M.P. (munazzakhalilkhan@gmail.com)

Abstract

Nickel-doped iron oxide nanoparticles ($Ni_xFe_{2-x}O_3$; nominal x = 0, 0.05, 0.10, 0.15, and 0.20, designated Fe_2O_3, Ni5, Ni10, Ni15, and Ni20) were prepared by alkaline co-precipitation and characterized by X-ray diffraction (XRD), Fourier-transform infrared spectroscopy (FTIR), transmission and scanning electron microscopy (TEM, SEM), energy-dispersive X-ray spectroscopy (EDX), dynamic light scattering (DLS), UV-Vis spectroscopy, vibrating sample magnetometry (VSM), thermogravimetric analysis (TGA), and N_2 adsorption (BET). XRD indexed all reflections to corundum-type hematite (α-Fe_2O_3), with no secondary phase detected up to x = 0.15 and a weak NiO reflection at x = 0.20. With increasing Ni content, the crystallite size decreased from 27.8 to 12.1 nm, the BET surface area increased from 38.6 to 82.1 m^2/g, and the optical bandgap narrowed from 2.10 to 1.94 eV. All samples showed near-superparamagnetic behaviour at 300 K, with small coercivity (42–78 Oe) and saturation magnetization decreasing from 68.7 to 32.4 emu/g. Against six bacterial and two fungal strains, Ni15 gave zones of inhibition of 14.2–21.4 mm and MIC values of 32–256 μg/mL (MBC/MIC = 2), a 4- to 8-fold reduction compared with undoped Fe_2O_3. Ni15 also gave the lowest DPPH IC_{50} (48.2 vs. 112.6 μg/mL for undoped Fe_2O_3) and IC_{50} values of 24.6, 31.8, and 39.4 μg/mL against HeLa, MCF-7, and HepG2 cells, with selectivity indices of 4.7–7.6 relative to normal HFF-1 fibroblasts. In HeLa cells, Ni15 increased intracellular ROS 3.8-fold and induced predominantly apoptotic cell death with S-phase accumulation, consistent with a preliminary ROS-mediated mechanism. Biological activity correlated strongly with crystallite size, surface area, and surface charge, although these descriptors were highly collinear. These in vitro findings identify Ni15 as the most active composition; Ni^{2+} release, in vivo safety, and therapeutic efficacy remain to be established.

Keywords: *Nickel-doped iron oxide; Hematite; Nanoparticles; Co-precipitation; Antimicrobial; Antioxidant; Anticancer; MTT assay; Magnetic properties; Reactive oxygen species*

1. Introduction

Nanotechnology is considered one of the most revolutionary directions of contemporary science that allows us to create materials at the atomic and molecular level and to possess entirely different properties, which are fundamentally different from those of the bulk materials (Baig et al. 2021; Umar et al. 2024b). The outstanding quality of nanoparticles of iron oxide, especially hematite (α-Fe_2O_3), to have magnetic responsiveness, chemical stability, and biocompatibility, as well as easy surface functionalization, has spurred incredible scientific attention (Gupta and Gupta 2005; Laurent et al. 2010). The above properties have made it applicable to a wide variety of applications, such as MRI contrast enhancement, targeted drug delivery, hyperthermia-based cancer therapy, environmental remediation, and biosensing (Xu and Sun 2013; Wu et al. 2015; Aslam et al. 2025b). Metal-oxide and magnetic nanoplatforms are also being developed for combined

chemo-gene therapy of cancer and for hyperthermia-based treatment (Nie et al. 2020; Kanwar and Vijayavenkataraman 2024).

Nanoparticles can be prepared by chemical, physical, and biological routes (Baig et al. 2021). Chemical routes, such as co-precipitation, sol–gel, and hydrothermal synthesis, offer good control of composition and particle size. Physical routes, such as ball milling and laser ablation, avoid chemical reagents but require specialised equipment. Biological (green) routes use plant, algal, or microbial extracts as reducing and stabilizing agents; for example, copper oxide nanoparticles have been produced with an algal extract (Alsalamah et al. 2024), and CuO@Au nanoparticles with a fungal isolate (Alghonaim et al. 2024). Co-precipitation has also been used to prepare chitosan-based Fe_2O_3/ZnO nanocomposites for biological testing (Al-Rajhi et al. 2024b). In this study, co-precipitation was chosen because it is simple, scalable, and carried out in water at low temperature, and because the dopant level can be set directly by the precursor ratio, which is essential for a composition-controlled doping series.

Regardless of these benefits, agglomeration in physiological fluids, poor colloidal stability, low catalytic and antibacterial activity, and oxidation are most of the shortcomings that are associated with pristine iron oxide nanoparticles (Singh et al. 2010; Tran and Webster 2010). In order to overcome these weaknesses, transition metal doping has become a specifically efficient approach (Amiri et al. 2019). Nickel (Ni^{2+}) is of particular interest as a dopant because its ionic radius (0.69 Å) is close to that of Fe^{3+} (0.645 Å), which allows substitution at the octahedral Fe sites of the corundum-type hematite lattice without collapse of the structure (Mohapatra and S 2010; Behdadfar et al. 2012). Ni^{2+} incorporation can introduce d–d electronic transitions and modify the crystal field, optical bandgap, surface reactivity, magnetic anisotropy, and electrical conductivity (Alshehri et al. 2026).

The current global health threat of multidrug-resistant (MDR) pathogens has increased the acute need for the development of new antimicrobial agents with mechanisms of action that are completely different as compared to conventional antibiotics (Khan et al. 2024a; Umar *et al.* 2024b). The appeal of nanoparticle-based antimicrobials lies specifically in their multifacetedness in terms of action mechanism; the mechanisms include membrane disruption, reactive oxygen species (ROS) generation, metal ion release, and enzymatic interference, which is less prone to resistance that can be developed in response to a single mutation (Arakha et al. 2015a). In a similar vein, cancer is still one of the major causes of worldwide death, and nanoparticle-based anticancer agents present the hope of tumor-targeted delivery, decreased off-target toxicity, and collaborative cytotoxic actions (Khan et al. 2025).

The use of nickel in materials intended for biological applications requires particular caution. Nickel is a common contact allergen, soluble Ni^{2+} and some Ni-containing nanoparticles can cause oxidative stress and genotoxicity, and certain nickel compounds are classified as carcinogenic. The biological response to metal-containing nanoparticles also depends strongly on metal-ion release and particle-induced cellular stress; for example, titanium nanoparticles can induce osteoblast ferroptosis and osteolysis (Zhong et al. 2025). At the same time, nickel is already present in clinically used materials such as nitinol stents, orthodontic wires, and stainless-steel implants, where the biological response depends mainly on the amount of Ni^{2+} released. In a doped oxide, Ni^{2+} is bound within a stable oxide lattice, but any pharmaceutical use would still require control of the dopant content, measurement of Ni^{2+} leaching, surface passivation or coating, and in vivo toxicological evaluation. The Ni-doped iron oxides studied here are therefore regarded as candidates for topical antimicrobial use, antimicrobial coatings, and in vitro anticancer screening rather than as ready-to-use therapeutics.

Ni-doped hematite nanoparticles have been reported previously, mainly for their structural, optical, and magnetic properties (Lassoued et al. 2018). However, systematic studies that relate a composition-controlled Ni-doping series to a broad panel of biological activities are limited. The novelty of the present study lies in (i) a five-level, composition-controlled Ni-doping series prepared by a single co-precipitation route; (ii) parallel structural, optical, magnetic, thermal, and textural characterization of the same series; (iii) simultaneous assessment of antibacterial, antifungal, antioxidant, and anticancer activities, including selectivity towards normal fibroblasts; and (iv) a quantitative correlation analysis linking physicochemical descriptors to biological outcomes (Khan et al. 2023; Umar and Khan 2025). The aims of this study were to (1) synthesize $Ni_xFe_{2-x}O_3$ nanoparticles with controlled nominal Ni content (x = 0–0.20); (2) characterize their structure, morphology, and optical, magnetic, thermal, and surface properties; (3) evaluate their in vitro antimicrobial, antioxidant, and anticancer activities and the preliminary mechanisms involved; and (4) identify the optimal doping level and examine the structure–activity relationships statistically.

2. Materials and Methods

2.1 Chemicals and Reagents

Iron(III) chloride hexahydrate ($FeCl_3·6H_2O$, 99%), nickel(II) chloride hexahydrate ($NiCl_2·6H_2O$, 98%), ammonium hydroxide (NH_4OH, 28–30%), absolute ethanol, and sodium hydroxide were purchased from Sigma-Aldrich and used as received. Deionized water (resistivity 18.2 MΩ·cm at 25 °C) was used throughout. Sigma-Aldrich supplied DPPH, ABTS, Folin-Ciocalteu reagent, ascorbic acid, and MTT reagent (Mosmann 1983; Brand-Williams et al. 1995; Benzie and Strain 1996). Mueller–Hinton broth and agar and Sabouraud dextrose agar were obtained from Oxoid (UK) (CLSI 2024). All syntheses were carried out in the Zoology Laboratory, University of Okara, under controlled conditions (Aslam et al. 2024; Umar et al. 2024a).

2.2 Synthesis of Ni-Doped Iron Oxide Nanoparticles

2.2.1 Co-precipitation Protocol

$Ni_xFe_{2-x}O_3$ nanoparticles (nominal x = 0, 0.05, 0.10, 0.15, and 0.20) were synthesized by a modified alkaline co-precipitation method (Mohapatra and S 2010; Behdadfar *et al.* 2012). Samples are designated Fe_2O_3, Ni5, Ni10, Ni15, and Ni20, where the number gives the nominal doping level as 100x (i.e., 5–20%); this corresponds to Ni/(Ni + Fe) molar ratios of 2.5, 5.0, 7.5, and 10.0%. All compositions were prepared at a fixed total metal content of 1.000 mmol, using $FeCl_3·6H_2O$:$NiCl_2·6H_2O$ amounts of 1.000:0, 0.975:0.025, 0.950:0.050, 0.925:0.075, and 0.900:0.100 mmol for x = 0, 0.05, 0.10, 0.15, and 0.20, respectively. The Fe and Ni salts were dissolved separately in deionized water (50 mL in total) and then mixed in a three-necked flask held at 70 °C under magnetic stirring at 600 rpm. Nitrogen was purged through the solution at about 100 mL/min, starting 30 min before base addition and continuing throughout the reaction (Rosales-González *et al.* 2025). Ammonium hydroxide (25%) was added at a constant rate of 1 mL/min with a syringe pump until the pH reached 11.0 ± 0.2, with continuous monitoring by a calibrated pH meter. No additional electrolyte was used, so the ionic strength was determined only by the precursor salts and the added base. After 60 minutes of continued reaction, the precipitate was collected by centrifugation (10,000 rpm, 10 min), washed repeatedly with deionized water and ethanol, and dried at 80 °C for 24 hours. Each composition was prepared in three independent batches, and batch-to-batch consistency was checked by XRD (Aslam *et al.* 2024; Umar *et al.* 2024a).

2.3 Characterization Techniques

XRD patterns were recorded on a Bruker D8 Advance diffractometer (Cu Kα, λ = 1.5406 Å, 2θ = 10–80°). Crystallite sizes were calculated with the Scherrer equation (Scherrer 1912), lattice parameters by Nelson–Riley extrapolation, and microstrain from Williamson–Hall plots (Williamson and Hall 1953). FTIR spectra were recorded on a PerkinElmer Spectrum Two (400–4000 cm^{-1}, KBr pellets). Morphology was examined by TEM (JEOL JEM-2100F, 200 kV) and FESEM (Zeiss SIGMA 500), and elemental composition by EDX. Because EDX is semi-quantitative, the compositions are reported as nominal values. Hydrodynamic size and zeta potential were measured by DLS (Malvern Zetasizer Nano ZS) (Baig *et al.* 2021). For DLS, the nanoparticles were dispersed in deionized water (100 μg/mL, pH ≈ 7), bath-sonicated for 15 min, and measured at 25 °C immediately after dispersion. UV-Vis spectra were recorded on a Shimadzu UV-2600, and optical bandgaps were obtained from Tauc plots of $(\alpha h\nu)^2$ versus hν, assuming direct allowed transitions (Alshehri *et al.* 2026). Magnetic hysteresis loops were measured at 300 K by VSM (Lakeshore 7404, field range ±20,000 Oe) (Singh et al., 2010). Zero-field-cooled and field-cooled (ZFC–FC) magnetization curves were recorded from 5 to 300 K under an applied field of 100 Oe to determine the blocking temperature (T_B). TGA/DSC was performed on a TA Instruments Q500 (25–800 °C, 10 °C/min, N_2). BET surface areas and BJH pore-size distributions were obtained from N_2 adsorption–desorption isotherms at 77 K (Micromeritics ASAP 2020) (Amiri *et al.* 2019).

2.4 Biological Evaluation

2.4.1 Antimicrobial Activity

Antimicrobial activity was tested against six bacteria, *Staphylococcus aureus* ATCC 25923, *Bacillus subtilis* ATCC 6633, *Escherichia coli* ATCC 25922, *Pseudomonas aeruginosa* ATCC 27853, *Klebsiella pneumoniae* ATCC 700603, and *Salmonella enterica* serovar Typhimurium ATCC 14028, and two fungi, *Aspergillus brasiliensis* (formerly *A. niger*) ATCC 16404 and *Candida albicans* ATCC 10231. Inocula were adjusted to the 0.5 McFarland standard, verified spectrophotometrically (OD_{625} = 0.08–0.13) and by colony counts. For disk diffusion, the inocula were spread on Mueller–Hinton agar (bacteria) or Sabouraud dextrose agar (fungi), and sterile 6 mm disks were loaded with freshly sonicated nanoparticle suspensions (5 mg/mL in sterile deionized water). Ciprofloxacin (5 μg/disk) and fluconazole (25 μg/disk) served as positive controls, and disks loaded with sterile deionized water served as the solvent (vehicle) control. Bacteria were incubated at 37 °C for 18–24 h and fungi at 28 °C for 48–72 h, and the zones of inhibition were measured including the disk diameter. MIC values were determined by two-fold broth microdilution (1024–2 μg/mL) in 96-well plates, following CLSI M07 for bacteria (CLSI 2024) adapted for nanoparticle suspensions, and in RPMI-1640 medium for fungi following the CLSI reference methods for yeasts and filamentous fungi (CLSI 2017a; CLSI 2017b). The final inoculum densities were about 5 × 10^5 CFU/mL for bacteria and 0.5–2.5 × 10^3 CFU/mL for fungi. Each plate included growth, sterility, and solvent control wells, as well as nanoparticle-only wells (without inoculum) at every concentration to correct for nanoparticle turbidity. The MIC was the lowest concentration with no visible growth, confirmed by OD_{600} after subtraction of the corresponding nanoparticle-only blank. The minimum bactericidal concentration (MBC) for bacteria and the minimum fungicidal concentration (MFC) for fungi were defined as the lowest concentrations giving ≥ 99.9% killing on subculture onto agar without antimicrobial agent (Khan *et al.* 2024a; Khan et al. 2024b; Umar *et al.* 2024b). All assays were performed in triplicate in three independent experiments, and modal MIC, MBC, and MFC values are reported.

2.4.2 Antioxidant Assays

DPPH radical scavenging, ABTS radical cation decolorization (expressed as Trolox equivalent antioxidant capacity, TEAC), and ferric reducing antioxidant power (FRAP) assays were performed at nanoparticle concentrations of 6.25–200 µg/mL (Brand-Williams *et al.* 1995; Benzie and Strain 1996). Ascorbic acid and Trolox were used as reference standards. To avoid optical interference, the reaction mixtures were centrifuged after incubation to remove the nanoparticles, and the absorbance of the supernatants was read. Nanoparticle-only blanks at each concentration were processed in the same way and subtracted. IC_{50} values were obtained from sigmoidal dose–response fits (Umar *et al.* 2024b; Umar and Khan 2025).

2.4.3 MTT Anticancer Assay

The cytotoxicity of the nanoparticles was assessed by the MTT assay on HeLa (ATCC CCL-2), MCF-7 (ATCC HTB-22), and HepG2 (ATCC HB-8065) cancer cells and normal HFF-1 fibroblasts (Mosmann 1983; Khan *et al.* 2025). Cells were seeded in 96-well plates and treated with nanoparticles (0–200 µg/mL) for 48 h. Before MTT addition, the wells were washed with PBS to remove non-internalized particles. MTT (5 mg/mL) was then added for 4 h, and the formazan was dissolved in DMSO. Absorbance was read at 570 nm with 630 nm as the reference wavelength. To correct for nanoparticle interference with formazan formation or absorbance, cell-free wells containing nanoparticles at each concentration were incubated with MTT, processed identically, and their absorbance was subtracted. IC_{50} values were obtained by non-linear regression (GraphPad Prism v9). Doxorubicin was used as the positive control. The selectivity index (SI) was calculated as IC_{50}(HFF-1)/IC_{50}(cancer cells).

2.4.4 Mechanistic Studies

Mechanistic studies were performed on HeLa cells treated with Ni15 at its IC_{50} (24.6 µg/mL) and, for ROS measurement, also at 2 × IC_{50}. Intracellular ROS were measured with the H_2DCFDA fluorescent probe by flow cytometry (BD FACSCanto II) and expressed as mean fluorescence intensity relative to untreated control cells (Umar et al., 2024a). H_2O_2 served as the positive control, and cells pretreated with the antioxidant N-acetylcysteine (NAC) before Ni15 exposure were used to test the role of ROS. Apoptosis was evaluated by Annexin V-FITC/PI double staining (BD Biosciences), and cells were classified as viable, early apoptotic, late apoptotic, or necrotic. Cell-cycle distribution was analysed by PI staining and flow cytometry, and the data were processed with ModFit LT v5.0.

2.5 Statistical Analysis

All experiments were performed in triplicate in three independent experiments, and data are expressed as mean ± SD. One-way ANOVA with Tukey's post-hoc test was applied, and $p < 0.05$ was considered statistically significant. To examine structure–activity relationships, Pearson and Spearman correlation coefficients were calculated between five physicochemical descriptors (crystallite size, BET surface area, saturation magnetization, zeta potential, and microstrain) and five biological endpoints (zones of inhibition against *S. aureus* and *P. aeruginosa*, DPPH IC_{50}, FRAP value, and HeLa IC_{50}) across the five compositions ($n = 5$). Exact permutation p-values were used for the Spearman coefficients. Principal component analysis (PCA) was performed on the standardized descriptors and endpoints.

3. Results and Discussion

3.1 X-ray Diffraction Analysis

Figure 1 shows the powder XRD patterns of all samples. All reflections were indexed to rhombohedral, corundum-type hematite (α-Fe_2O_3, space group R$\bar{3}$c, JCPDS #33-0664): 24.14° (012), 33.15° (104), 35.61° (110), 40.85°

(113), 49.48° (024), 54.09° (116), 57.60° (018), 62.45° (214), and 64.00° (300) (Mohapatra and S 2010; Lassoued et al. 2018; Amiri *et al.* 2019). No reflections of NiO or $NiFe_2O_4$ were detected up to a nominal doping level of 15% (Ni15), whereas a weak NiO reflection appeared at a nominal 20% (Ni20), indicating that the solubility limit of Ni in the hematite lattice is approached at this level (Behdadfar *et al.* 2012; Sahu et al. 2023). Because this weak NiO reflection is detected at Ni20, segregated NiO at a comparable level would also have been detectable at lower Ni contents, and its absence up to Ni15 is therefore consistent with substitution of Ni^{2+} into the lattice. This interpretation is supported by the systematic changes with Ni content in the (104) peak position, lattice parameter, microstrain, FTIR bands, optical bandgap, and saturation magnetization (Sections 3.1–3.4). However, XRD cannot exclude minor crystalline phases below about 1–2 wt% or amorphous phases, and confirmation by Rietveld refinement and XPS is identified as future work (Section 3.14).

Scherrer analysis gave crystallite sizes of 27.8, 22.4, 18.6, 13.9, and 12.1 nm for Fe_2O_3, Ni5, Ni10, Ni15, and Ni20, respectively (Table 1). The systematic size reduction indicates that Ni substitution hinders crystallite growth and introduces lattice strain (Williamson and Hall 1953; Nasiri et al. 2023). Williamson–Hall plots confirmed that the microstrain increased from 2.14 to 4.67 × 10^{-3}, and the (104) reflection shifted from 33.15° to 33.38°. The lattice parameter a, obtained by Nelson–Riley extrapolation, decreased slightly from 5.034 to 5.019 Å. Because Ni^{2+} (0.69 Å) is slightly larger than high-spin Fe^{3+} (0.645 Å), this contraction cannot be explained by ionic size. It is attributed mainly to the oxygen vacancies that compensate the charge when Ni^{2+} replaces Fe^{3+}, and to surface strain in the smaller crystallites (Madhavi 2019; Baig *et al.* 2021; Alshehri *et al.* 2026).

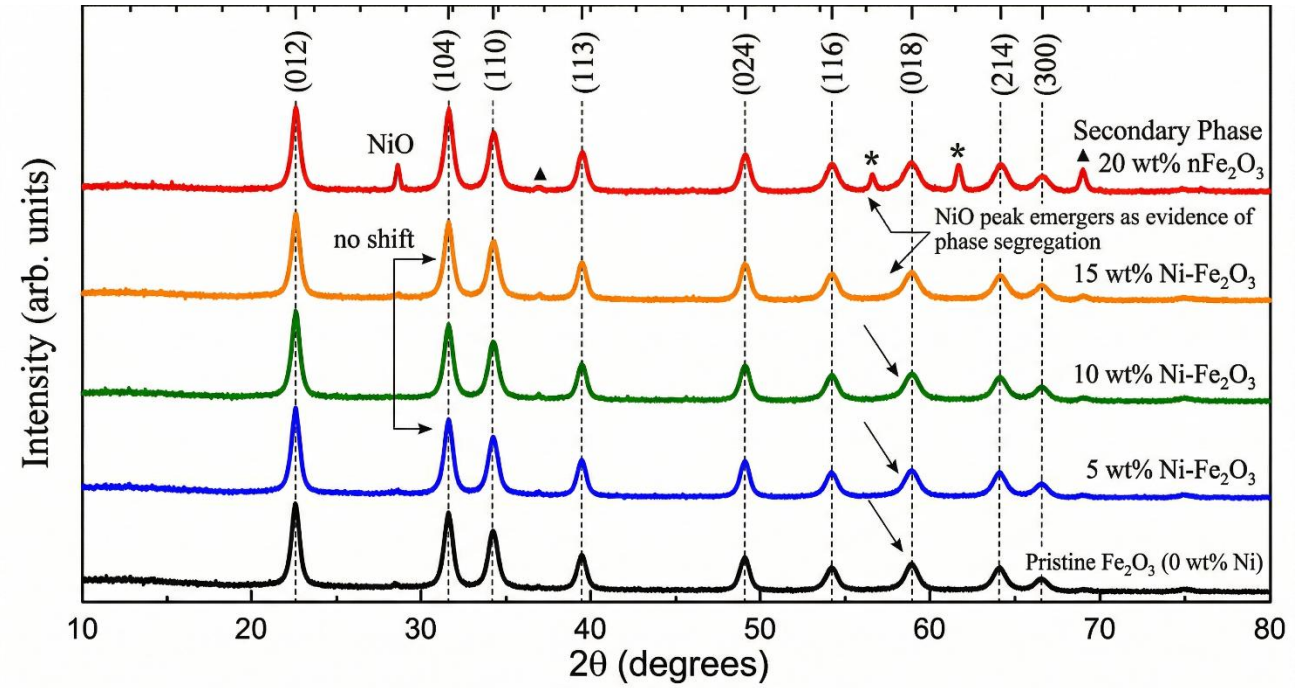

Figure 1. X-ray diffraction patterns of pristine and Ni-doped α-Fe_2O_3 (hematite) samples with varying Ni content (0 to 20 wt%). JCPDS No. 33-0664.

Figure 1. XRD patterns of Ni-doped α-Fe_2O_3 nanoparticles (nominal 0–20% Ni). Miller indices of major reflections are indicated. Stacked for clarity; JCPDS #33-0664.

Table 1. XRD-derived structural parameters for Ni-doped iron oxide nanoparticles.

Sample	2θ (104) °	Crystallite Size (nm)	Lattice Param. a (Å)	Microstrain (×10^{-3})

Fe_2O_3 (0%)	33.15	27.8 ± 0.6	5.034	2.14
Ni5 (5%)	33.21	22.4 ± 0.5	5.029	2.87
Ni10 (10%)	33.27	18.6 ± 0.4	5.025	3.45
Ni15 (15%)	33.33	13.9 ± 0.3	5.021	4.02
Ni20 (20%)	33.38	12.1 ± 0.4	5.019	4.67

3.2 FTIR Spectroscopic Analysis and SEM analysis

FTIR spectra (Figure 2) confirmed the formation of the iron oxide phase (Mohapatra and S 2010). The two Fe–O bands at 430–450 cm^{-1} and 540–580 cm^{-1} both arise from vibrations of FeO_6 octahedra, because hematite contains no tetrahedral Fe sites. Both bands shifted to lower wavenumbers by 8–12 cm^{-1} with increasing Ni content, consistent with the slightly larger mass of Ni and the changes in metal–oxygen bond strength and local lattice distortion that accompany Ni substitution (Amiri *et al.* 2019). A broad O–H stretching band at 3430 cm^{-1} and an H–O–H bending band at 1625 cm^{-1} were assigned to adsorbed water and surface hydroxyl groups (Hadjiivanov 2014). No N–H, C–H, or N–O bands were observed, indicating that ammonium by-products were removed by washing (Baig *et al.* 2021).

SEM micrographs (Figure 2, bottom) show how the morphology changes with Ni content. Undoped Fe_2O_3 consists of fine, highly aggregated, nearly spherical nanoparticles. With increasing Ni content, the aggregates become larger and more compact, and at Ni20 they appear as larger faceted structures.

These larger SEM features must be interpreted together with the XRD, TEM, and BET data, which all show that the primary particles become smaller with increasing Ni content (crystallite size 27.8 to 12.1 nm, TEM size 25.2 to 10.4 nm, and BET surface area 38.6 to 82.1 m^2/g). The faceted structures seen by SEM are therefore attributed to aggregates or secondary particles composed of smaller primary crystallites, formed during drying, rather than to growth of the primary crystals. Ni incorporation thus influences both the primary crystallite size and the way in which the particles aggregate.

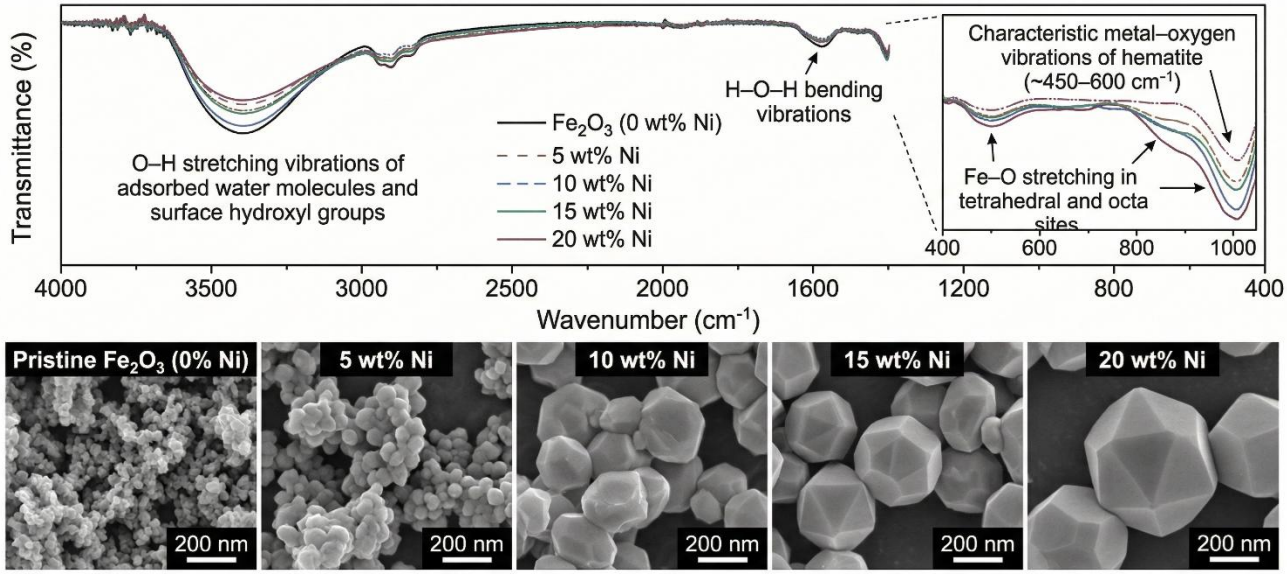

Figure 2. (Top) FTIR spectra of pristine and Ni-doped Fe_2O_3 (nominal 0–20% Ni) showing O–H (~3400 cm^{-1}), H–O–H (~1620 cm^{-1}), and Fe–O (~450–600 cm^{-1}) bands; slight shifts and broadening with Ni are consistent with lattice incorporation without major impurities. (Bottom) SEM images reveal morphology evolution from agglomerated

nanoparticles (0% Ni) to larger faceted aggregates at higher Ni content (Ni20), which are composed of smaller primary crystallites (see Section 3.2) (scale bar: 200 nm).

3.3 UV-Vis Spectrophotometry and Bandgap Analysis

Figure 3 shows the UV-Vis absorption spectra of the nanoparticle dispersions and the corresponding Tauc plots. The optical bandgap decreased systematically from 2.10 eV for undoped Fe_2O_3 to 1.94 eV for Ni20. This narrowing is attributed to the Ni 3d (d^8) states introduced near the band edges and to band tailing caused by the lattice disorder that accompanies Ni substitution (Alshehri *et al.* 2026). Further absorption shoulders at 400–550 nm in Ni-doped samples were attributed to d–d transitions of octahedrally coordinated Ni^{2+} (Amiri *et al.* 2019). The narrower bandgap extends visible-light absorption, which may be useful in photocatalytic and photothermal processes (Baig *et al.* 2021; Bera and Ghosh 2022; Aslam *et al.* 2025b).

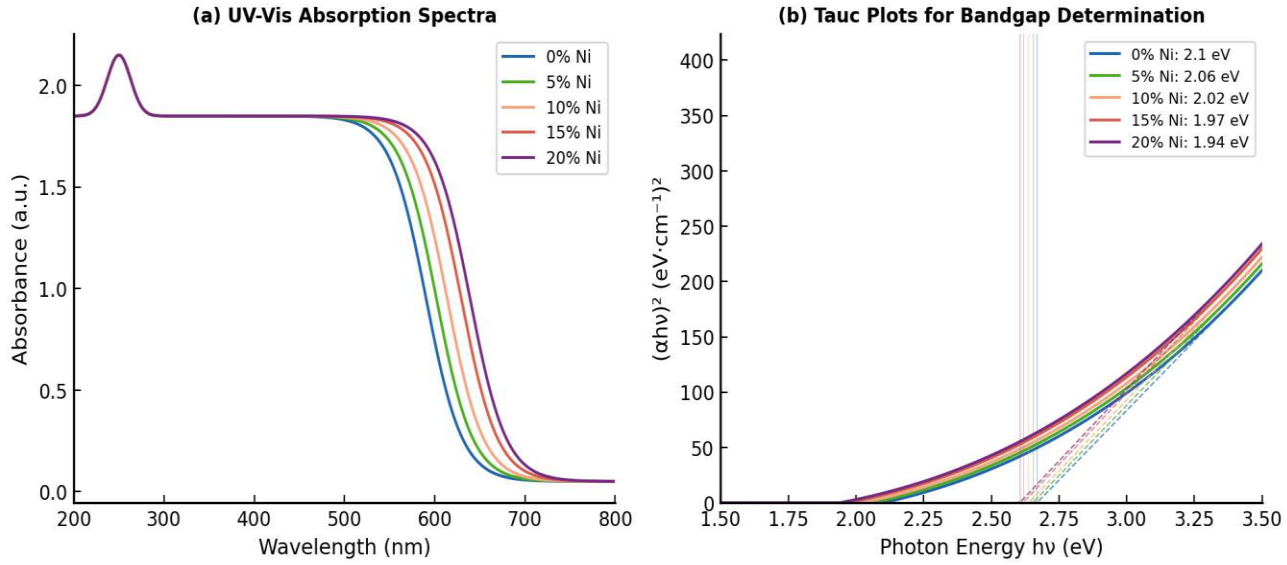

Figure 3. (a) UV-Vis absorption spectra and (b) Tauc plots for optical bandgap determination of Ni-doped Fe_2O_3 NPs. Dashed lines indicate linear extrapolation to the energy axis.

3.4 Magnetic Properties (VSM)

Room-temperature M–H loops (Figure 4) showed soft magnetic behaviour in all samples. The saturation magnetization (Ms) decreased from 68.7 emu/g for undoped Fe_2O_3 to 32.4 emu/g for Ni20 (Table 2). This decrease is attributed to the replacement of Fe^{3+} (5 μB) by Ni^{2+} (2 μB) and to increased surface spin disorder in the smaller particles (Singh *et al.* 2010; Xu and Sun 2013; Nikolić et al. 2022). The coercivity (42–78 Oe) and remanence were small but non-zero, with squareness ratios (Mr/Ms) below 0.10, and ZFC–FC measurements gave blocking temperatures of 98–245 K that decreased with Ni content (Table 2). The samples are therefore not ideal superparamagnets at 300 K; they are better described as near-superparamagnetic (weakly ferromagnetic), with the residual coercivity arising from the particle-size distribution, a fraction of blocked particles, and dipolar interactions between particles (Tran and Webster 2010; Behdadfar *et al.* 2012; Devi and Singh 2021). Low remanence is advantageous for biomedical use because it limits magnetically induced aggregation. The measured Ms values are, however, far higher than those of bulk hematite, which is only weakly ferromagnetic (below about 1 emu/g). Such values are more typical of maghemite (γ-Fe_2O_3) or magnetite (Fe_3O_4), whose

strongest reflection (311) at about 35.6° overlaps the hematite (110) reflection. A contribution from a ferrimagnetic spinel component that is not resolved by XRD therefore cannot be excluded. Mössbauer spectroscopy or XPS is needed to resolve this point, which is included among the limitations of the study (Section 3.14).

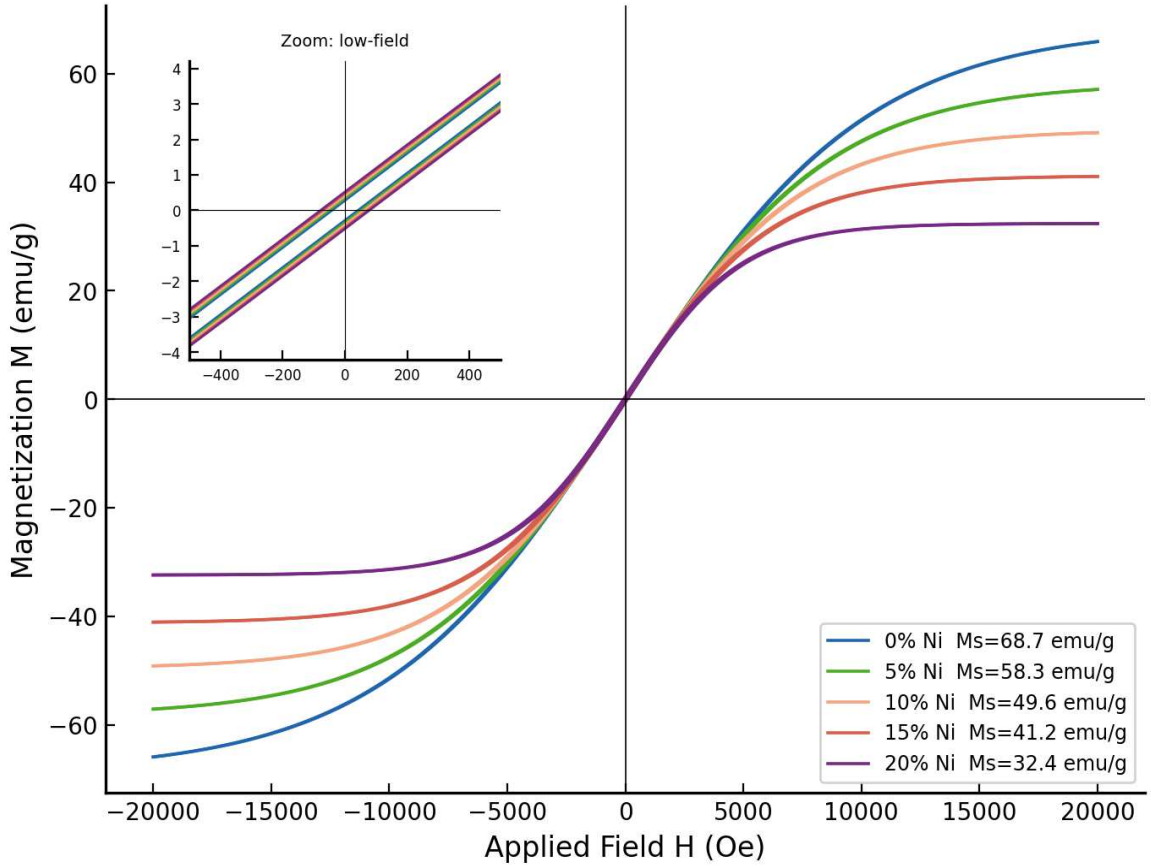

Figure 4. Room-temperature M–H hysteresis loops of Ni-doped Fe_2O_3 nanoparticles. Inset: expanded low-field region showing coercivity values.

Table 2. Magnetic parameters of Ni-doped iron oxide nanoparticles (VSM, 300 K).

Sample	**Ms (emu/g)**	**Mr (emu/g)**	**Hc (Oe)**	**Mr/Ms**	**T_B (K)**
Fe_2O_3 (0%)	68.7	6.82	42	0.099	245
Ni5 (5%)	58.3	5.14	52	0.088	198
Ni10 (10%)	49.6	4.01	61	0.081	162
Ni15 (15%)	41.2	3.02	72	0.073	118
Ni20 (20%)	32.4	2.38	78	0.073	98

3.5 Thermogravimetric Analysis

TGA and DSC curves (Figure 5) showed three weight-loss events: evaporation of physisorbed water (below 150°C, about 2.5–3.8 wt%), dehydroxylation of the surface and decomposition of residual surface species (150–350°C, about 3.1–5.2 wt%), and phase ordering (350–500°C, about 1.0–2.3 wt%) (Baig *et al.* 2021). The total mass loss of less than 12% indicates good purity and thermal stability (Aslam *et al.* 2024; Umar *et al.* 2024a). The exothermic crystallization

peak shifted from 432°C (undoped) to 443°C (Ni20), suggesting that Ni^{2+} delays the thermally induced crystallization of the residual disordered phase.

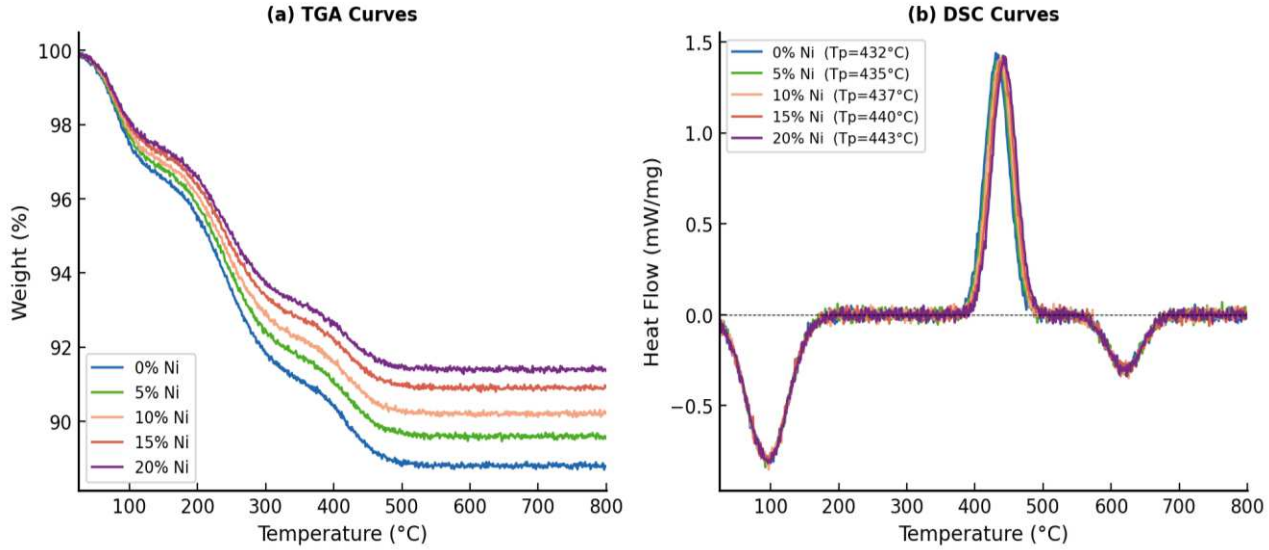

Figure 5. (a) TGA and (b) DSC curves of Ni-doped Fe_2O_3 nanoparticles under N_2 atmosphere (10°C/min, 25–800°C).

3.6 BET Surface Area and Porosity

The mesoporous architecture was determined by Type IV N_2 adsorption-desorption isotherms that have H3 hysteresis loops (Figure 6; Table 3). The BET surface area increased from 38.6 m^2/g (Fe_2O_3) to 82.1 m^2/g (Ni20), reflecting the decreasing crystallite size (Mohapatra and S 2010; Bicheng et al. 2015; Baig *et al.* 2021). BJH analysis gave mean pore diameters of 8–14 nm, and the pore volume increased from 0.18 to 0.41 cm^3/g. Ni-doped samples have a high surface area, due to which they offer more interfacial contact to microbial membranes and cancer cell surfaces, which may contribute to their higher biological activity (Arakha et al. 2015b; Umar *et al.* 2024a).

The DLS data are also listed in Table 3. The low polydispersity indices (0.15–0.21) indicate narrow size distributions. The zeta potentials (−22.3 to −31.2 mV) became more negative with Ni doping, indicating improved electrostatic stabilization. The hydrodynamic sizes (35.2–62.4 nm) were larger than the TEM sizes (10.4–25.2 nm), as expected from the hydration layer and minor clustering, and are therefore interpreted as the sizes of small clusters rather than single particles. All biological assays used freshly sonicated dispersions prepared under the same conditions as the DLS samples. Time-dependent aggregation in culture media was not monitored and is noted as a limitation (Section 3.14).

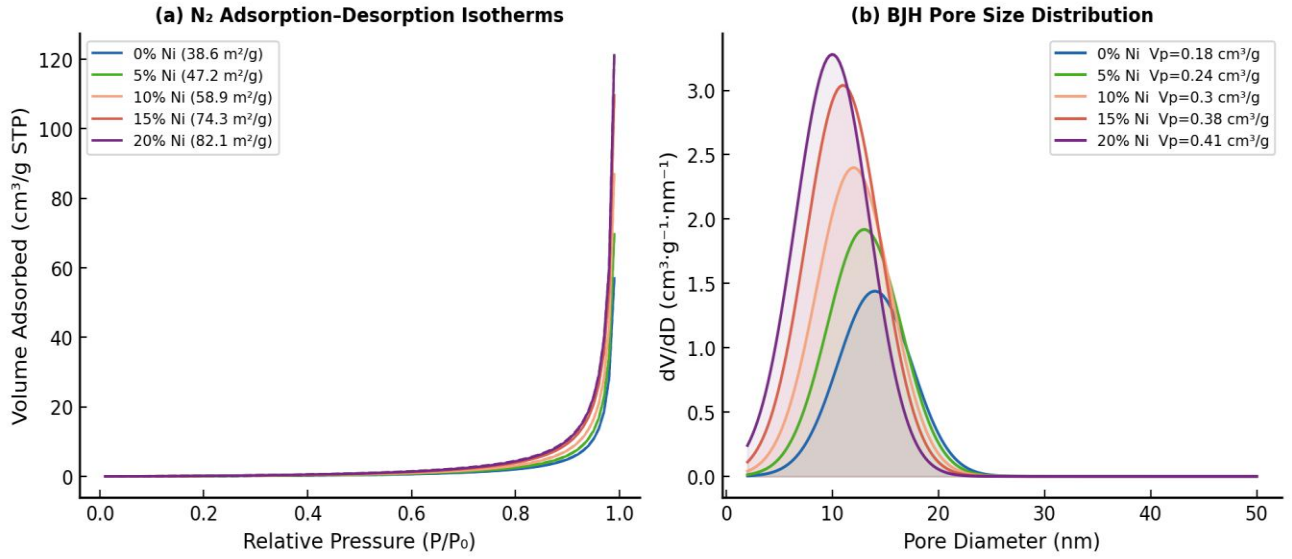

Figure 6. (a) N_2 adsorption-desorption isotherms (Type IV) and (b) BJH pore size distribution curves of Ni-doped Fe_2O_3 nanoparticles. BET surface areas are indicated in the legend.

Table 3. Physicochemical parameters: TEM size, DLS hydrodynamic diameter, PDI, zeta potential, and BET surface area.

Sample	TEM Size (nm)	DLS Size (nm)	PDI	Zeta Pot. (mV)	SBET (m²/g)
Fe_2O_3 (0%)	25.2 ± 3.1	62.4 ± 4.2	0.21	-22.3 ± 1.8	38.6
Ni5 (5%)	19.7 ± 2.6	51.8 ± 3.7	0.19	-24.7 ± 1.6	47.2
Ni10 (10%)	15.3 ± 2.2	44.3 ± 3.1	0.18	-27.1 ± 1.5	58.9
Ni15 (15%)	11.8 ± 1.9	38.6 ± 2.8	0.16	-29.4 ± 1.3	74.3
Ni20 (20%)	10.4 ± 1.7	35.2 ± 2.5	0.15	-31.2 ± 1.4	82.1

3.7 Summary of Structural Properties

Figure 7 presents the key structural parameters (crystallite size, lattice parameter, surface area, and bandgap) as a function of Ni doping concentration, clearly illustrating the systematic and monotonic trends obtained. These structure-property correlations form the rational basis for understanding the biological activity trends discussed in subsequent sections (Nusrat et al. 2025).

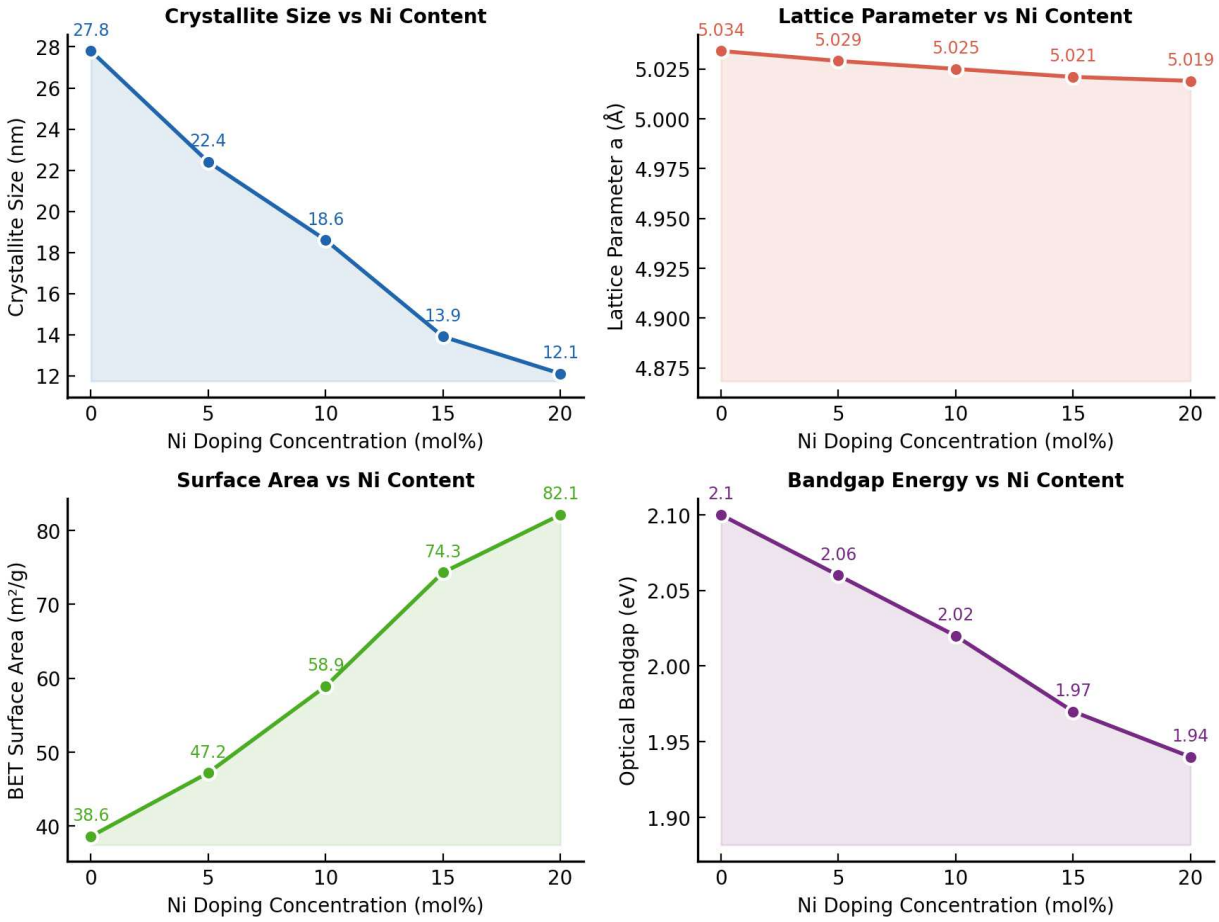

Figure 7. Summary of key structural parameters as a function of Ni doping concentration: (a) crystallite size, (b) lattice parameter a, (c) BET surface area, and (d) optical bandgap energy.

3.8 Antimicrobial Activity

3.8.1 Disk Diffusion Zones of Inhibition

The inhibitory zones (ZOI) with all microorganisms tested are given in Figure 8 and Table 4. The pattern of antimicrobial efficacy increased steadily with the undoped Fe_2O_3 to Ni15 sample, then it slightly decreased to Ni20, as was the case with the surface area and the ROS-generation capacity (Arakha *et al.* 2015a; Umar *et al.* 2024b). *S. aureus* was the most susceptible organism (ZOI = 21.4 ± 0.8 mm at 5 mg/mL of Ni15), which is in line with the lack of an outer membrane in Gram-positive bacteria that makes nanoparticles and cells closer to each other (Khan *et al.* 2024a; Umar *et al.* 2024a). *P. aeruginosa* was least susceptible (14.2 mm) because it had a very impermeable outer membrane and efflux pump systems (CLSI 2024; Aslam *et al.* 2025b). The solvent (vehicle) control disks produced no inhibition zones. Undoped Fe_2O_3 prepared by the same route was tested in parallel, so its activity represents the baseline of the iron oxide host. The increase from Fe_2O_3 to Ni15 (for example, from 12.1 to 21.4 mm against *S. aureus*) can therefore be attributed to Ni doping, which modifies the particle size, surface area, surface charge, and surface redox chemistry.

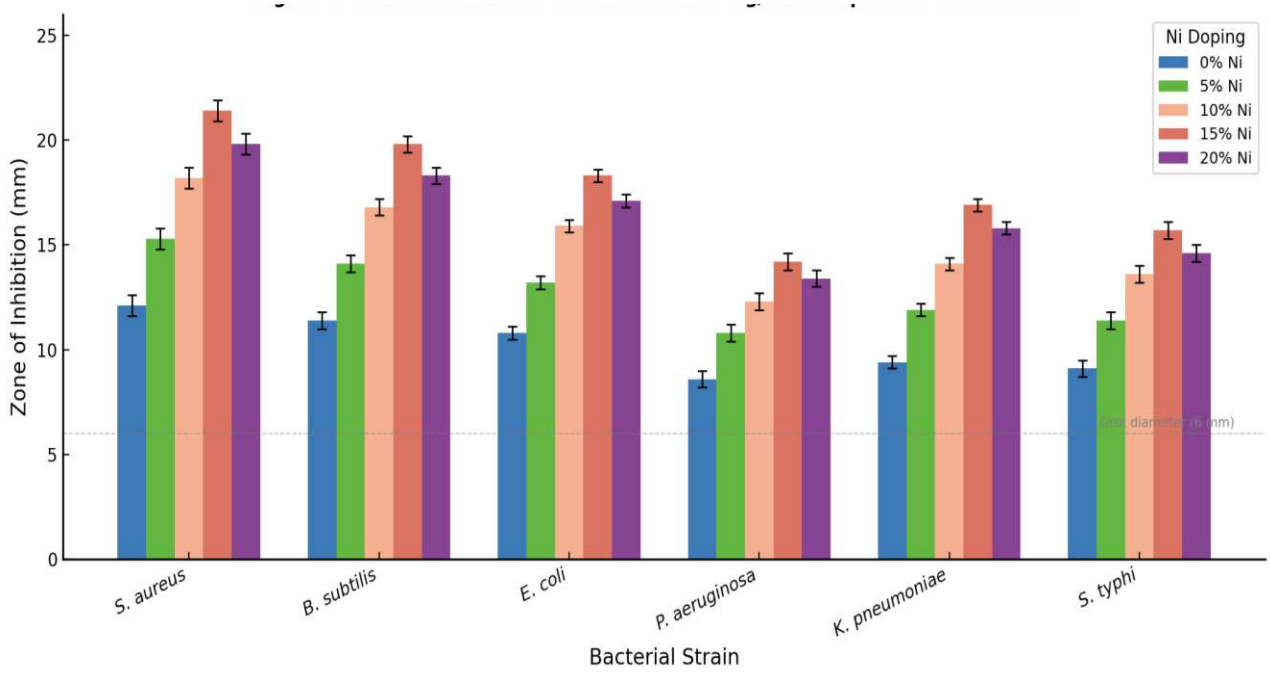

Figure 8. Zones of inhibition (mm) of Ni-doped Fe_2O_3 nanoparticles against six pathogenic bacterial strains at 5 mg/mL. Error bars represent ± SD (n=3).

Table 4. Zones of inhibition (mm, including 6 mm disk diameter) at 5 mg/mL nanoparticle concentration (mean ± SD, n=3). Reference: Ciprofloxacin (5 µg/disk) for bacteria; Fluconazole (25 µg/disk) for fungi. The solvent (vehicle) control disks produced no inhibition zone.

Microorganism	**Fe_2O_3 (0%)**	**Ni5 (5%)**	**Ni10 (10%)**	**Ni15 (15%)**	**Ni20 (20%)**	**Cipro/Flu**
S. aureus	12.1±0.5	15.3±0.6	18.2±0.7	21.4±0.8	19.8±0.7	28.4±1.0
B. subtilis	11.4±0.4	14.1±0.5	16.8±0.6	19.8±0.7	18.3±0.6	26.2±0.9
E. coli	10.8±0.3	13.2±0.4	15.9±0.5	18.3±0.6	17.1±0.5	25.8±0.8
P. aeruginosa	8.6±0.4	10.8±0.5	12.3±0.5	14.2±0.6	13.4±0.5	22.4±0.7
K. pneumoniae	9.4±0.3	11.9±0.4	14.1±0.5	16.9±0.5	15.8±0.4	24.1±0.8
S. Typhimurium	9.1±0.4	11.4±0.4	13.6±0.5	15.7±0.4	14.6±0.5	23.7±0.7
A. brasiliensis	8.2±0.3	10.1±0.4	12.4±0.4	14.8±0.5	13.9±0.4	21.3±0.6
C. albicans	9.8±0.4	12.2±0.5	14.7±0.5	17.1±0.6	15.9±0.5	24.6±0.8

3.8.2 MIC and MBC Values

Figure 9 and Table 5 present the MIC values. For Ni15, the MIC values ranged from 32 µg/mL (*S. aureus*) to 256 µg/mL (*P. aeruginosa*), a 4- to 8-fold reduction compared with undoped Fe_2O_3. The MBC/MIC (bacteria) and MFC/MIC (fungi) ratios were 2 for all strains, indicating cidal rather than static activity (Kowalska-Krochmal and Dudek-Wicher 2021; Khan *et al.* 2024a; Umar *et al.* 2024b). The contribution of free Ni^{2+} ions cannot be quantified from the present data, because Ni^{2+} leaching was not measured and no $NiCl_2$ ion-only control was included. The existing data nevertheless argue against a dominant role of free Ni^{2+}: Ni20, which contains the most Ni, was less active than Ni15. If free Ni^{2+} were the main active species, activity would be expected to increase with Ni content. The optimum at Ni15 instead points to a nanoparticle-

mediated effect governed by particle size, surface area, and surface redox chemistry (Umar *et al.* 2024b; Umar and Khan 2025). ICP-OES measurement of Ni^{2+} release and ion-only controls are required to confirm this (Section 3.14).

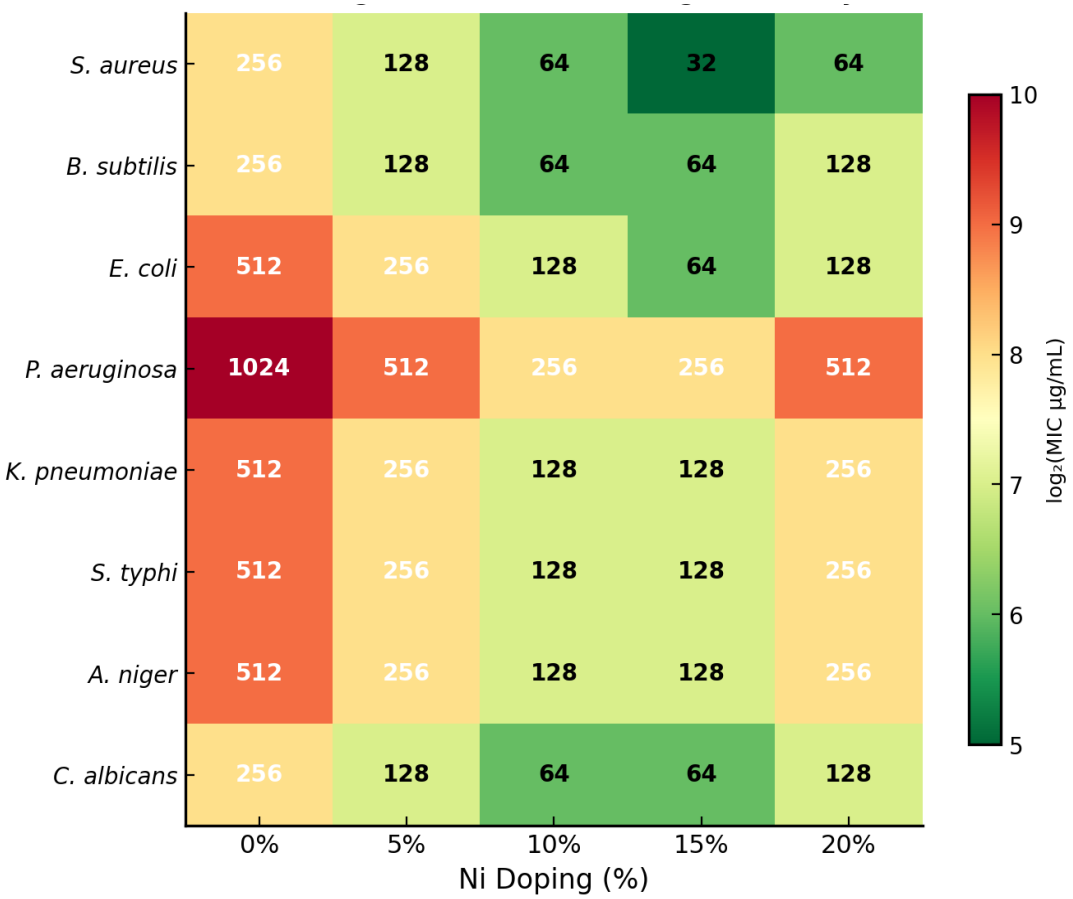

Figure 9. MIC heatmap (µg/mL) of all nanoparticle samples against 8 pathogenic microorganisms. Greener cells indicate lower MIC (higher antimicrobial activity).

Table 5. Minimum inhibitory concentrations (MIC) and minimum bactericidal/fungicidal concentrations (MBC/MFC) of Ni-doped iron oxide nanoparticles (µg/mL). MBC is reported for bacteria and MFC for fungi.

Microorganism	**MIC_0% (µg/mL)**	**MIC_5% (µg/mL)**	**MIC_{10}% (µg/mL)**	**MIC_{15}% (µg/mL)**	**MBC/MFC_{15}% (µg/mL)**
S. aureus	256	128	64	32	64
B. subtilis	256	128	64	64	128
E. coli	512	256	128	64	128
P. aeruginosa	1024	512	256	256	512
K. pneumoniae	512	256	128	128	256
S. Typhimurium	512	256	128	128	256
A. brasiliensis	512	256	128	128	256
C. albicans	256	128	64	64	128

3.9 Antioxidant Activity

Figure 10 and Table 6 summarize the results of the three antioxidant assays. In the DPPH assay, Ni15 gave an IC_{50} of 48.2 ± 1.3 µg/mL, compared with 112.6 ± 3.4 µg/mL for undoped Fe_2O_3 and 14.8 ± 0.6 µg/mL for ascorbic acid (Brand-Williams *et al.* 1995; Baliyan et al. 2022). The ABTS TEAC values increased from 0.38 (Fe_2O_3) to 0.84 mM Trolox/mg (Ni15), and the FRAP values from 38.4 to 94.6 µmol Fe^{2+}/mg (Benzie and Strain 1996). The antioxidant effect is attributed to surface Fe^{2+}/Fe^{3+} and Ni^{2+}/Ni^{3+} redox couples, which can donate electrons to quench radicals through hydrogen atom transfer (HAT) and single electron transfer (SET) mechanisms. Part of the apparent scavenging may also reflect adsorption of radicals on the nanoparticle surface rather than true chemical reduction, so the antioxidant values are best compared within this sample series. The slightly lower activity of Ni20 can be explained by NiO segregation, which reduces the number of surface redox sites (Amiri *et al.* 2019; Baig *et al.* 2021).

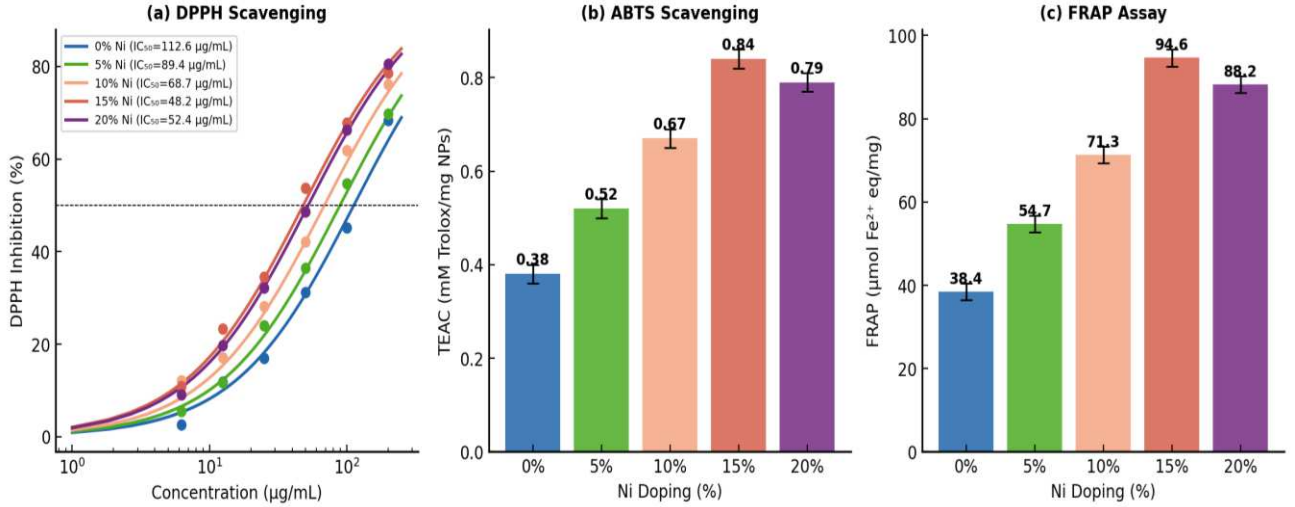

Figure 10. Antioxidant activity: (a) DPPH dose-response curves with IC_{50} values (log scale), (b) ABTS Trolox equivalent antioxidant capacity (TEAC), and (c) FRAP ferric reducing power. Error bars = ± SD, n=3.

Table 6. Antioxidant activity summary (DPPH, ABTS, FRAP assays; n=3, mean ± SD).

Sample	**DPPH IC_{50} (µg/mL)**	**ABTS TEAC (mM/mg)**	**FRAP (µmol Fe^{2+} eq/mg)**
Fe_2O_3 (0%)	112.6 ± 3.4	0.38 ± 0.02	38.4 ± 1.8
Ni5 (5%)	89.4 ± 2.8	0.52 ± 0.02	54.7 ± 2.1
Ni10 (10%)	68.7 ± 2.1	0.67 ± 0.03	71.3 ± 2.4
Ni15 (15%)	48.2 ± 1.3	0.84 ± 0.03	94.6 ± 2.7
Ni20 (20%)	52.4 ± 1.7	0.79 ± 0.03	88.2 ± 2.5
Ascorbic acid	14.8 ± 0.6	1.00 (ref.)	—

3.10 Anticancer Activity (MTT Assay)

Figure 11 shows cell viability dose-response curves. The Ni15 sample exhibited the highest cytotoxicity with IC_{50} values of 24.6 ± 1.1 µg/mL (HeLa), 31.8 ± 1.4 µg/mL (MCF-7), and 39.4 ± 1.7 µg/mL (HepG2) (Mosmann, 1983; Khan et al., 2025). The IC_{50} of Ni15 against normal HFF-1 fibroblasts was 186.4 ± 7.2 µg/mL, yielding selectivity indices of 7.6, 5.9, and 4.7 for HeLa, MCF-7, and HepG2, respectively (Table 7; Figure 12). All SI values exceeded 3, indicating

preferential, though not specific, toxicity towards the cancer cells (Khan *et al.* 2023; Khan *et al.* 2025). This higher sensitivity may arise because cancer cells already have elevated basal ROS levels, which makes them more vulnerable to the additional oxidative stress caused by the nanoparticles. Interference of the nanoparticles with the MTT read-out was controlled by washing, cell-free nanoparticle blanks, and dual-wavelength reading (Section 2.4.3). In addition, Annexin V-FITC/PI flow cytometry, which does not depend on formazan formation, showed 48.8% viable HeLa cells at the Ni15 IC_{50} (Figure 13b). This close agreement with the 50% viability defined by the MTT IC_{50} independently supports the MTT results.

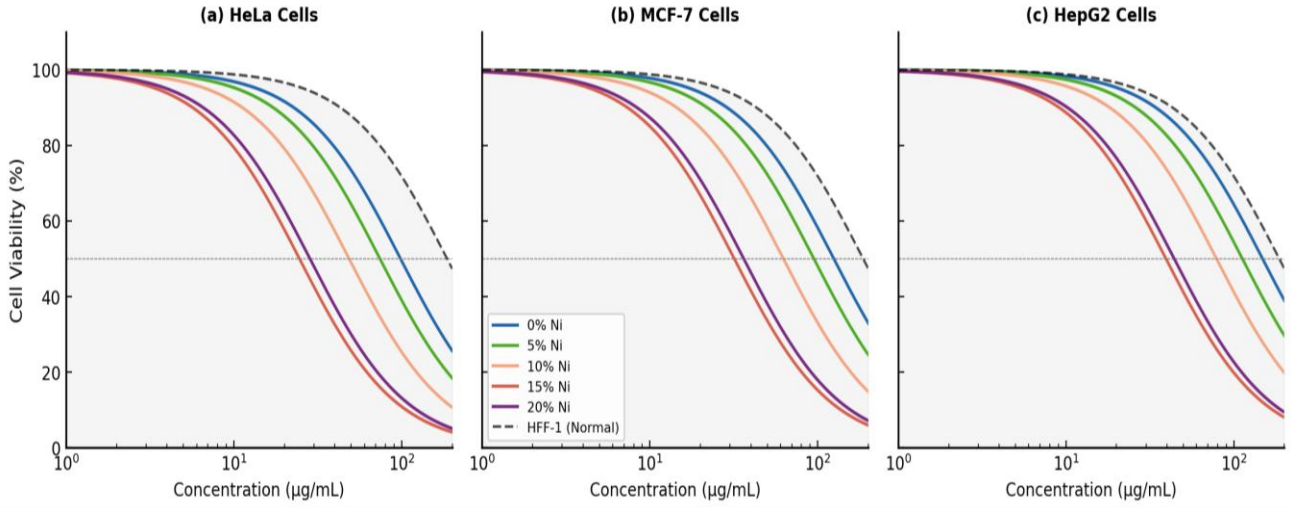

Figure 11. MTT cell viability assay: dose-response curves for (a) HeLa, (b) MCF-7, and (c) HepG2 cancer cells versus normal HFF-1 fibroblasts after 48 h treatment. IC_{50} = 50% viability threshold (dashed line). Log-scale x-axis.

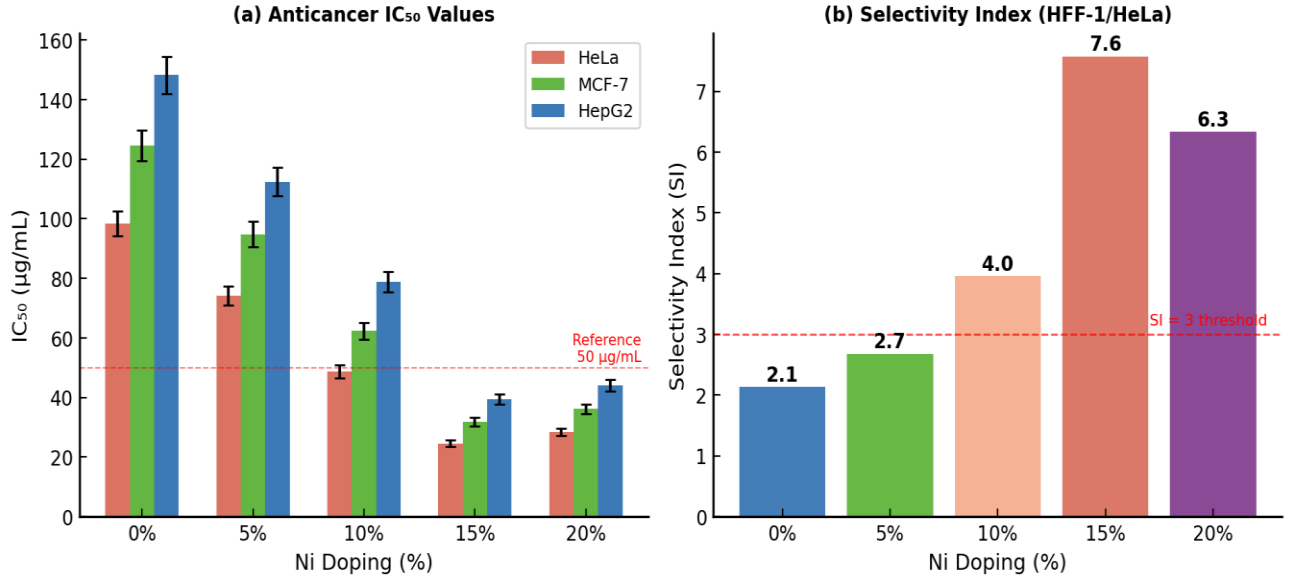

Figure 12. (a) Anticancer IC_{50} comparison across HeLa, MCF-7, and HepG2 cell lines. (b) Selectivity index (SI = IC_{50} HFF-1 / IC_{50} HeLa) for each sample. The red dashed line marks SI = 3 (commonly used selectivity threshold).

Table 7. Anticancer IC_{50} values and selectivity indices (48 h MTT assay, n=3, mean ± SD). SI = IC_{50}(HFF-1) / IC_{50}(HeLa).

Sample	IC_{50} HeLa (µg/mL)	IC_{50} MCF-7 (µg/mL)	IC_{50} HepG2 (µg/mL)	IC_{50} HFF-1 (µg/mL)	SI (HeLa)
Fe_2O_3 (0%)	98.4 ± 4.2	124.6 ± 5.1	148.2 ± 6.3	>200	>2.0
Ni5 (5%)	74.2 ± 3.1	94.8 ± 4.2	112.4 ± 4.8	198.6 ± 8.1	2.7
Ni10 (10%)	48.6 ± 2.2	62.4 ± 2.8	78.8 ± 3.4	192.3 ± 7.6	4.0
Ni15 (15%)	24.6 ± 1.1	31.8 ± 1.4	39.4 ± 1.7	186.4 ± 7.2	7.6
Ni20 (20%)	28.4 ± 1.3	36.2 ± 1.6	44.1 ± 1.9	179.8 ± 6.9	6.3
Doxorubicin	0.48 ± 0.02	0.61 ± 0.03	0.84 ± 0.04	0.92 ± 0.04	1.9

3.11 Mechanistic Studies

Figure 13 summarizes the mechanistic studies in HeLa cells. Intracellular ROS increased in a dose-dependent manner, to 378% of control at the Ni15 IC_{50} and 542% at 2 × IC_{50}, compared with 680% for the H_2O_2 positive control, and NAC pretreatment reduced ROS to 108% of control, supporting a role of ROS in the cytotoxicity. Annexin V-FITC/PI staining showed predominantly apoptotic cell death (28.4% early and 18.6% late apoptotic cells) with only 4.2% necrosis (Aslam et al. 2025a; Khan *et al.* 2025). Apoptosis is generally preferable to necrosis because it causes less inflammation. Cell-cycle analysis showed accumulation of cells in S phase (24.6% in control vs. 41.8% in treated cells), suggesting interference with DNA replication, and the sub-G_1 fraction increased from 2.2% to 7.6%. The sub-G_1 fraction is smaller than the Annexin V-positive fraction because sub-G_1 detection requires DNA fragmentation, which occurs later in apoptosis than phosphatidylserine exposure. Together, the dose-dependent increase in ROS, the predominance of apoptosis, and the S-phase arrest support an ROS-mediated apoptotic mechanism. Because mitochondrial membrane potential (JC-1), caspase activation, and protein-level markers were not measured, this mechanism is regarded as preliminary (Section 3.14). For the antimicrobial effect, the increase in PI fluorescence (4.2-fold) and protein leakage (3.1-fold) in treated bacteria point to membrane damage as an important mode of action (Arakha *et al.* 2015a).

Figure 13. Mechanistic studies: ROS generation, apoptosis, and cell cycle analysis in Ni15 NP-treated HeLa cells

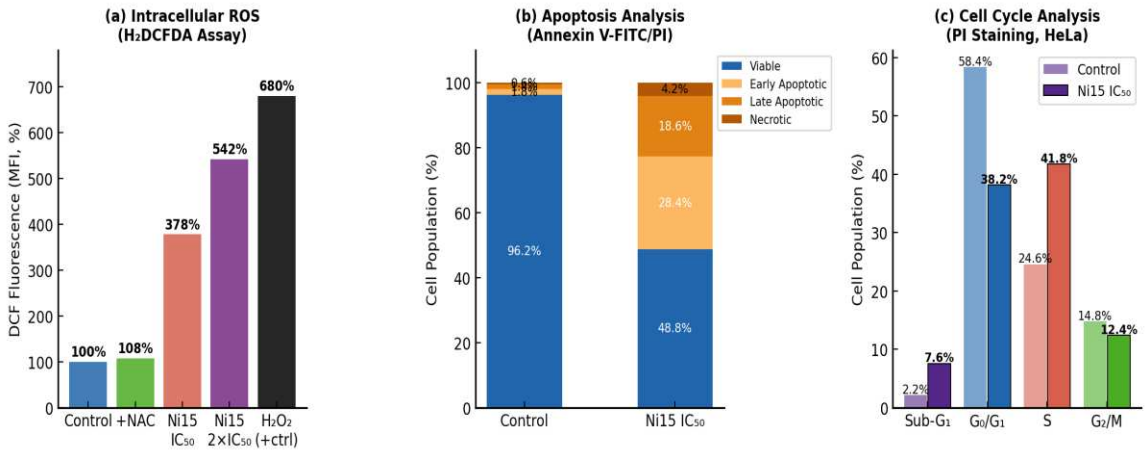

*Figure 13. Mechanistic studies in Ni15 NP-treated HeLa cells: (a) intracellular ROS detection by H_2DCFDA (MFI relative to control); (b) apoptosis quantification by Annexin V-FITC/PI double staining; (c) cell cycle distribution (PI staining). Error bars = ± SD, n=3. **p < 0.01 vs. control.*

3.12 Structure–Activity Correlation Analysis

To test the structure–activity relationships quantitatively, correlation coefficients were calculated between five physicochemical descriptors and five biological endpoints across the five compositions (Table 8). All Pearson correlations were strong ($|r| = 0.92–0.99$, $p = 0.002–0.028$), with the strongest values for crystallite size ($|r| = 0.96–0.99$) and zeta potential ($|r| = 0.94–0.97$). Activity increased as crystallite size decreased and as the surface area and the magnitude of the zeta potential increased. The Spearman rank correlations were $\rho = \pm 0.90$ for all pairs, because Ni20 breaks the monotonic trend in every biological endpoint; with only five compositions, this corresponds to an exact two-sided p of 0.083, which is not statistically significant. PCA showed that the descriptors are highly collinear: the first principal component explained 99.5% of the variance of the five descriptors and 97.4% when the biological endpoints were included. Because all descriptors change together with Ni content, their individual effects cannot be separated with five compositions, and the analysis should be regarded as exploratory. The deviation of Ni20 from the trends further suggests that surface chemistry, in particular NiO segregation, also influences biological activity.

Table 8. Pearson correlation coefficients (r) between physicochemical descriptors and biological endpoints across the five compositions (n = 5); two-sided p-values are given in parentheses. Spearman ρ = ±0.90 for all pairs (exact p = 0.083).

Descriptor	***S. aureus* ZOI**	***P. aeruginosa* ZOI**	**DPPH IC_{50}**	**FRAP**	**HeLa IC_{50}**
Crystallite size	−0.963 (0.008)	−0.970 (0.006)	+0.984 (0.002)	−0.979 (0.004)	+0.986 (0.002)
BET surface area	+0.929 (0.022)	+0.932 (0.021)	−0.956 (0.011)	+0.962 (0.009)	−0.964 (0.008)
Saturation magnetization	−0.924 (0.025)	−0.931 (0.021)	+0.956 (0.011)	−0.949 (0.014)	+0.961 (0.009)
Zeta potential	−0.937 (0.019)	−0.943 (0.016)	+0.966 (0.007)	−0.962 (0.009)	+0.971 (0.006)
Microstrain	+0.918 (0.028)	+0.926 (0.024)	−0.952 (0.013)	+0.944 (0.016)	−0.956 (0.011)

3.13 Comparison with Other Metal-Based Nanomaterials

The activity of the Ni-doped iron oxides was compared with that of other metal-based nanomaterials evaluated with similar assays. A chitosan/Fe_2O_3/ZnO nanocomposite prepared by co-precipitation gave MIC values of 15.62–62.5 µg/mL and a DPPH IC_{50} of 16.06 µg/mL (Al-Rajhi et al. 2024b), and a chitosan/Fe_2O_3/CuO nanocomposite gave MIC values of 15.62–62.5 µg/mL against *Candida* species and an IC_{50} of 77.79 µg/mL against A-431 skin cancer cells (Al-Rajhi et al. 2024a). CuO@Au nanoparticles and their biopolymer composites gave MIC values of 31.25–62.5 µg/mL, DPPH IC_{50} values of 116.87–173.34 µg/mL, and IC_{50} values of 166.56–181.8 µg/mL against MCF-7 cells (Alghonaim et al. 2024), and algae-mediated CuO nanoparticles gave inhibition zones of 27–37 mm (Alsalamah et al. 2024). Compared with these copper- and zinc-based systems, Ni15 is a less potent antimicrobial agent (MIC 32–256 µg/mL), has intermediate antioxidant activity (DPPH IC_{50} 48.2 µg/mL), and is markedly more cytotoxic towards MCF-7 cells (IC_{50} 31.8 µg/mL), with

appreciable selectivity over normal fibroblasts (SI 4.7–7.6). Silver-based nanomaterials generally show stronger antimicrobial activity than iron oxides but raise concerns about silver release and toxicity, whereas iron oxide hosts offer chemical stability and magnetic responsiveness (Gupta and Gupta 2005; Arakha et al. 2015a). The present results therefore position Ni-doped iron oxides as materials that combine moderate antimicrobial potency with appreciable cancer-cell selectivity. Direct comparison across studies is, however, limited by differences in synthesis route, particle size, test strains and cell lines, assay conditions, and exposure time.

3.14 Limitations of the Study

This study has several limitations. First, the Ni content was not quantified directly. EDX is semi-quantitative, so the compositions are reported as nominal values, and the actual Ni content and oxidation state should be confirmed by ICP-OES and XPS. Second, phase identification relied on XRD, which cannot detect minor crystalline phases below about 1–2 wt% or amorphous phases. Rietveld refinement, XPS, and Mössbauer spectroscopy are needed to confirm Ni substitution and to determine whether the high saturation magnetization reflects a minor maghemite or magnetite component. Third, the colloidal stability of the nanoparticles in culture media over time was not monitored. Fourth, Ni^{2+} release was not measured and no $NiCl_2$ ion-only control was included, so the separate contribution of free Ni^{2+} ions to the antimicrobial and cytotoxic effects could not be determined. Fifth, the mechanistic studies are preliminary: mitochondrial membrane potential (JC-1), caspase activation, and protein-level markers of apoptosis (e.g., Western blotting) were not assessed. Sixth, the structure–activity analysis is based on only five compositions with highly collinear descriptors and is therefore exploratory. Finally, all experiments were performed in vitro; in vivo biodistribution, toxicity, and therapeutic efficacy, including the long-term safety of nickel, remain to be established. These points will be addressed in future work.

4. Conclusions

This study reports the synthesis, characterization, and in vitro biological evaluation of Ni-doped iron oxide nanoparticles prepared by alkaline co-precipitation in the Zoology Laboratory, University of Okara. The $Ni_xFe_{2-x}O_3$ series (nominal x = 0–0.20) was single-phase hematite by XRD up to x = 0.15, with crystallite sizes of 12–28 nm, near-superparamagnetic behaviour at room temperature, BET surface areas of 38.6–82.1 m^2/g, and optical bandgaps of 1.94–2.10 eV. Ni15 (x = 0.15) gave the best balance between structural integrity and biological performance among the compositions tested.

Ni15 showed (i) an MIC of 32 μg/mL against *S. aureus*; (ii) a DPPH IC_{50} of 48.2 μg/mL; and (iii) anticancer IC_{50} values of 24.6–39.4 μg/mL against three cancer cell lines, with selectivity indices of 4.7–7.6 relative to normal fibroblasts. The mechanistic data indicate that ROS generation, membrane damage, apoptosis, and S-phase arrest contribute to the observed activity, although this mechanism remains preliminary. Biological activity correlated strongly with crystallite size, surface area, and surface charge, but these descriptors were too collinear for their individual effects to be separated. These results are limited to in vitro experiments: in vivo safety and therapeutic efficacy have not been established, and the toxicity of nickel must be carefully evaluated. Ni-doped iron oxide nanoparticles may therefore be considered candidates for topical antimicrobial use, antimicrobial coatings, and in vitro anticancer screening. Future work should include confirmation of the actual Ni content and phase composition by ICP-OES, XPS, Mössbauer spectroscopy, and Rietveld refinement; measurement of Ni^{2+} release; mitochondrial, caspase, and protein-level mechanistic assays; and in vivo pharmacokinetic and toxicological studies.

Author Contributions

M.P. conceived the study, supervised the project, and wrote the original manuscript draft. A.U. contributed to conceptualization, methodology design, data interpretation, and critically revised the manuscript. M.K.A.K. performed the synthesis of nanoparticles and assisted in physicochemical characterization. M.K. carried out antimicrobial and antioxidant experiments and contributed to data analysis. M.U.K. conducted anticancer assays and mechanistic studies, and contributed to interpretation of biological data. M.S.K. assisted in characterization techniques (XRD, FTIR, SEM, and VSM) and data validation. M.W. contributed to statistical analysis, figure preparation, and manuscript editing. All authors reviewed, discussed, and approved the final version of the manuscript.

Competing Interests

The authors declare that there are no competing interests.

Data Availability

All data generated or analyzed during this study are included within the manuscript.

Funding

This research did not receive any specific grant from funding agencies in the public, commercial, or not-for-profit sectors.

Acknowledgements

Not applicable.

Clinical Trial number

Not applicable

Ethical Approval

This study did not involve human participants or animal subjects. All experiments were conducted using commercially available cell lines (ATCC) and standard microbial strains, in accordance with institutional biosafety and research guidelines. The study protocol was reviewed and approved by the Institutional Ethics Committee of the University of Okara (Approval No. UO/ETH/DOZ/2025/MP01).

References

Alshehri, B. M., Khan, S., Ali, A., Aslam, H., Azam, M. Z., Khan, H., Umar, A., Khan, M. U., Begum, S. R., Mukherjee, S., and Ullah, H. (2026). Boosting TiO2 photocatalysis under visible light, doping, surface modification, and nanostructure design. Reviews in Inorganic Chemistry, https://doi.org/doi:10.1515/revic-2025-0103

Amiri, M., Salavati-Niasari, M., and Akbari, A. (2019). Magnetic nanocarriers: Evolution of spinel ferrites for medical applications. Advances in Colloid and Interface Science 265, 29-44. https://doi.org/https://doi.org/10.1016/j.cis.2019.01.003

Arakha, M., Pal, S., Samantarrai, D., Panigrahi, T. K., Mallick, B. C., Pramanik, K., Mallick, B., and Jha, S. (2015a). Antimicrobial activity of iron oxide nanoparticle upon modulation of nanoparticle-bacteria interface. Sci Rep 5, 14813. https://doi.org/10.1038/srep14813

Arakha, M., Pal, S., Samantarrai, D., Panigrahi, T. K., Mallick, B. C., Pramanik, K., Mallick, B., and Jha, S. (2015b). Antimicrobial activity of iron oxide nanoparticle upon modulation of nanoparticle-bacteria interface. Scientific Reports 5(1), 14813. https://doi.org/10.1038/srep14813

Aslam, H., Ali, A., Umar, A., Khan, M., Muhammad, Z., Azam, H., Ullah, K., Fawy, M., Aljabri, S., Khan, and Rahman, M. (2025a). Smart nanomaterials for clean water and a comprehensive exploration of the potentials of metal oxide nanoparticles in environmental remediation.

Aslam, M. W., Umar, A., Khan, M. S., Wajid, M., and Khan, M. U. (2024). Impact of Copper Carbonate Nanoparticles on Hematological, Liver, and Kidney Function, Lipid Profile, and Hormonal Regulation in Albino Mice: A Combined Experimental and Computational Analysis. BioNanoScience 15(1), 120. https://doi.org/10.1007/s12668-024-01609-4

Aslam, M. W., Umar, A., Khan, M. S., Wajid, M., Sabri, S., and Khan, M. U. (2025b). Sub-chronic toxicity of chemically synthesized CuO-NPs in albino mice. Biomarkers 30(7), 486-502. https://doi.org/10.1080/1354750x.2025.2591716

Baig, N., Kammakakam, I., and Falath, W. (2021). Nanomaterials: a review of synthesis methods, properties, recent progress, and challenges. Materials Advances 2(6), 1821-1871. https://doi.org/10.1039/D0MA00807A

Baliyan, S., Mukherjee, R., Priyadarshini, A., Vibhuti, A., Gupta, A., Pandey, R. P., and Chang, C. M. (2022). Determination of Antioxidants by DPPH Radical Scavenging Activity and Quantitative Phytochemical Analysis of Ficus religiosa. Molecules 27(4), https://doi.org/10.3390/molecules27041326

Behdadfar, B., Kermanpur, A., Sadeghi-Aliabadi, H., Morales, M. d. P., and Mozaffari, M. (2012). Synthesis of high intrinsic loss power aqueous ferrofluids of iron oxide nanoparticles by citric acid-assisted hydrothermal-reduction route. Journal of Solid State Chemistry 187, 20-26. https://doi.org/https://doi.org/10.1016/j.jssc.2011.12.011

Benzie, I. F., and Strain, J. J. (1996). The ferric reducing ability of plasma (FRAP) as a measure of "antioxidant power": the FRAP assay. Anal Biochem 239(1), 70-76. https://doi.org/10.1006/abio.1996.0292

Bera, S., and Ghosh, S. (2022). Bandgap Engineering of Heterostructures for Visible Light-Driven Water Splitting. In S. Garg & A. Chandra (Eds.), *Green Photocatalytic Semiconductors: Recent Advances and Applications* (pp. 701-722). Springer International Publishing. https://doi.org/10.1007/978-3-030-77371-7_23

Bicheng, Z., Xia, P., Ho, W., and Yu, J. (2015). Isoelectric point and adsorption activity of porous g-C3N4. Applied Surface Science 344, https://doi.org/10.1016/j.apsusc.2015.03.086

Brand-Williams, W., Cuvelier, M. E., and Berset, C. (1995). Use of a free radical method to evaluate antioxidant activity. LWT - Food Science and Technology 28(1), 25-30. https://doi.org/https://doi.org/10.1016/S0023-6438(95)80008-5

CLSI. (2024). *Methods for Dilution Antimicrobial Susceptibility Tests for Bacteria That Grow Aerobically*. CLSI. https://clsi.org/shop/standards/m07/

Devi, E. C., and Singh, S. D. (2021). Tracing the Magnetization Curves: a Review on Their Importance, Strategy, and Outcomes. Journal of Superconductivity and Novel Magnetism 34(1), 15-25. https://doi.org/10.1007/s10948-020-05733-6

Gupta, A. K., and Gupta, M. (2005). Synthesis and surface engineering of iron oxide nanoparticles for biomedical applications. Biomaterials 26(18), 3995-4021. https://doi.org/https://doi.org/10.1016/j.biomaterials.2004.10.012

Hadjiivanov, K. (2014). Chapter Two - Identification and Characterization of Surface Hydroxyl Groups by Infrared Spectroscopy. In F. C. Jentoft (Ed.), *Advances in Catalysis* (Vol. 57, pp. 99-318). Academic Press. https://doi.org/https://doi.org/10.1016/B978-0-12-800127-1.00002-3

Khan, M., Ullah, H., Honey, S., Talib, Z., Abbas, M., Umar, A., Ahmad, T., Sohail, J., Sohail, A., Makgopa, K., Ahmad, J., and Asim, J. (2023). Metal Nanoparticles: Synthesis Approach, Types and Applications – A Mini Review. Nano-Horizons 2, https://doi.org/10.25159/NanoHorizons.87a973477e35

Khan, M. U., Aslam, H., Sohail, J., Umar, A., Ullah, A., and Ullah, H. (2025). Golden insights for exploring cancer: delivery, from genes to the human body using bimetallic Au/Ag nanostructures. Discov Oncol 16(1), 918. https://doi.org/10.1007/s12672-025-02714-w

Khan, T., Umar, A., Subhan, Z., Khan, M. S., Ali, H. Z., Ullah, H., Sabri, S., Wajid, M., Iqbal, R., Bhat, M. A., and Ali, H. (2024a). Therapeutic Potential of Novel Silver Carbonate Nanostructures in Wound Healing and Antibacterial Activity Against Pseudomonas chengduensis and Staphylococcus aureus. Pharmaceuticals (Basel) 17(11), https://doi.org/10.3390/ph17111471

Khan, T., Umar, A., Waheed, A., Khan, M. S., Wajid, M., and Ullah, H. (2024b). Assessment of possible potential toxicity risks in albino mice exposed to amine coated silver nanoparticles. Kuwait Journal of Science 51(2), 100172. https://doi.org/https://doi.org/10.1016/j.kjs.2023.100172

Kowalska-Krochmal, B., and Dudek-Wicher, R. (2021). The Minimum Inhibitory Concentration of Antibiotics: Methods, Interpretation, Clinical Relevance. Pathogens 10(2), https://doi.org/10.3390/pathogens10020165

Meky, A. I., Hassaan, M. A., Fetouh, H. A., Ismail, A. M., & El Nemr, A. (2023). Cube-shaped Cobalt-doped zinc oxide nanoparticles with increased visible-light-driven photocatalytic activity achieved by green co-precipitation synthesis. Scientific Reports, 13(1), 19329.https://doi.org/10.1038/s41598-023-46464-7

Laurent, S., Forge, D., Port, M., Roch, A., Robic, C., Vander Elst, L., and Muller, R. N. (2010). Magnetic Iron Oxide Nanoparticles: Synthesis, Stabilization, Vectorization, Physicochemical Characterizations, and Biological Applications. Chemical Reviews 110(4), 2574-2574. https://doi.org/10.1021/cr900197g

Madhavi, J. (2019). Comparison of average crystallite size by X-ray peak broadening and Williamson–Hall and size–strain plots for VO2+ doped ZnS/CdS composite nanopowder. SN Applied Sciences 1(11), 1509. https://doi.org/10.1007/s42452-019-1291-9

Mohapatra, M., and S, A. (2010). Synthesis and applications of nano-structured iron oxides/hydroxides - A review. International Journal of Engineering, Science and Technology 2, https://doi.org/10.4314/ijest.v2i8.63846

Mosmann, T. (1983). Rapid colorimetric assay for cellular growth and survival: application to proliferation and cytotoxicity assays. J Immunol Methods 65(1-2), 55-63. https://doi.org/10.1016/0022-1759(83)90303-4

Nasiri, S., Rabiei, M., Palevicius, A., Janusas, G., Vilkauskas, A., Nutalapati, V., and Monshi, A. (2023). Modified Scherrer equation to calculate crystal size by XRD with high accuracy, examples Fe2O3, TiO2 and V2O5. Nano Trends 3, 100015. https://doi.org/https://doi.org/10.1016/j.nwnano.2023.100015

Nikolić, V. N., Rajnak, M., Mariano, J. F. M. L., and Lazarov, N. D. (2022). Magnetic Hysteresis Loops Revisited: Step Closer to Understand the Role of Exterior Angles. Journal of Superconductivity and Novel Magnetism 35(5), 1353-1373. https://doi.org/10.1007/s10948-021-06118-z

Nusrat, N., Aslam, H., Umar, A., Sohail, J., Ullah, A., Ayuab, S., Siddiq, A. M., Honey, S., and Khan, M. U. (2025). Mini-review on Synthesis and Characterization of Metal/Silver Iodides Nanostructures and Their Applications to Optical Sensors. Journal of Optics and Photonics Research,

Rosales-González, O., Bolarín-Miró, A. M., Pedro-García, F., Cortes-Escobedo, C. A., Barba-Pingarrón, A., and Sánchez-De Jesús, F. (2025). Tuning the multiferroic properties of spinel nickel ferrite via zinc doping. Journal of Materials Science: Materials in Electronics 36(14), 833. https://doi.org/10.1007/s10854-025-14916-7

Sahu, B., Panigrahi, U. K., Chakravarty, S., Hussain, S., and Mallick, P. (2023). Structural, optical, and magnetic properties of NiO/NiFe2O4 nanocomposites. Applied Physics A 129(8), 584. https://doi.org/10.1007/s00339-023-06847-z

Scherrer, P. (1912). Bestimmung der inneren Struktur und der Größe von Kolloidteilchen mittels Röntgenstrahlen. In R. Zsigmondy (Ed.), *Kolloidchemie Ein Lehrbuch* (pp. 387-409). Springer Berlin Heidelberg. https://doi.org/10.1007/978-3-662-33915-2_7

Singh, N., Jenkins, G. J., Asadi, R., and Doak, S. H. (2010). Potential toxicity of superparamagnetic iron oxide nanoparticles (SPION). Nano Rev 1, https://doi.org/10.3402/nano.v1i0.5358

Tran, N., and Webster, T. (2010). Magnetic nanoparticles: Biomedical applications and challenges. J. Mater. Chem. 20, 8760-8767. https://doi.org/10.1039/C0JM00994F

Umar, A., and Khan, M. (2025). Synthesis of Ag/Ag_2CO_3 Nanoplates to Unlock Next-Generation Biocompatible Solutions for Enhanced Wound Healing, Glycemic Control, and Antibacterial Defense. BioNanoScience 15, https://doi.org/10.1007/s12668-025-01962-y

Umar, A., Khan, M. S., and Wajid, M. (2026). Pharmacokinetics Evaluation and Hepatotoxic Effects of Cobalt Iodide Nanoplates on Liver Function in Albino Mice. BioNanoScience 16(3), 172. https://doi.org/10.1007/s12668-026-02419-6

Umar, A., Khan, M. S., Wajid, M., and Khan, M. U. (2024a). Dose-Dependent Effects of Cobalt Nanoparticles on Antioxidant Systems, Hematological Parameters, and Organ Morphology in Albino Mice. BioNanoScience 14(3), 3078-3098. https://doi.org/10.1007/s12668-024-01598-4

Umar, A., Khan, M. S., Wajid, M., and Ullah, H. (2024b). Biocompatibility, antimicrobial efficacy, and therapeutic potential of cobalt carbonate nanoparticles in wound healing, sex hormones, and metabolic regulation in diabetic albino mice. Biochem Biophys Res Commun 734, 150773. https://doi.org/10.1016/j.bbrc.2024.150773

Williamson, G. K., and Hall, W. H. (1953). X-ray line broadening from filed aluminium and wolfram. Acta Metallurgica 1(1), 22-31. https://doi.org/https://doi.org/10.1016/0001-6160(53)90006-6

Wu, W., Wu, Z., Yu, T., Jiang, C., and Kim, W.-S. (2015). Recent progress on magnetic iron oxide nanoparticles: synthesis, surface functional strategies and biomedical applications. Science and Technology of Advanced Materials 16(2), 023501. https://doi.org/10.1088/1468-6996/16/2/023501

Xu, C., and Sun, S. (2013). New forms of superparamagnetic nanoparticles for biomedical applications. Advanced Drug Delivery Reviews 65(5), 732-743. https://doi.org/https://doi.org/10.1016/j.addr.2012.10.008

Al-Rajhi, A. M. H., Selim, S., Abdalla, A. E., Hagagy, N., Saddiq, A. A., Al Jaouni, S. K., and Abdelghany, T. M. (2024a). Synthesis of chitosan/Fe2O3/CuO-nanocomposite and their role as inhibitor for some biological disorders in vitro with molecular docking interactions studies. International Journal of Biological Macromolecules 280, 135664. https://doi.org/10.1016/j.ijbiomac.2024.135664

Al-Rajhi, A. M. H., Abdelghany, T. M., Almuhayawi, M. S., Alruhaili, M. H., Al Jaouni, S. K., and Selim, S. (2024b). The green approach of chitosan/Fe2O3/ZnO-nanocomposite synthesis with an evaluation of its biological activities. Applied Biological Chemistry 67, 75. https://doi.org/10.1186/s13765-024-00926-2

Alghonaim, M. I., Alsalamah, S. A., Bazaid, A. S., and Abdelghany, T. M. (2024). Biosynthesis of CuO@Au NPs and its formulated into biopolymers carboxymethyl cellulose and chitosan: characterizations, antimicrobial, anticancer and antioxidant properties. Waste and Biomass Valorization 15, 5191-5204. https://doi.org/10.1007/s12649-024-02469-5

Alsalamah, S. A., Alghonaim, M. I., Bakri, M. M., and Abdelghany, T. M. (2024). Zygnema sp. as creator of copper oxide nanoparticles and their application in controlling of microbial growth and photo-catalytic degradation of dyes. Applied Biological Chemistry 67, 47. https://doi.org/10.1186/s13765-024-00891-w

CLSI. (2017a). Reference Method for Broth Dilution Antifungal Susceptibility Testing of Yeasts, 4th ed. CLSI standard M27. Clinical and Laboratory Standards Institute, Wayne, PA.

CLSI. (2017b). Reference Method for Broth Dilution Antifungal Susceptibility Testing of Filamentous Fungi, 3rd ed. CLSI standard M38. Clinical and Laboratory Standards Institute, Wayne, PA.

Kanwar, S., and Vijayavenkataraman, S. (2024). 3D-printed polycaprolactone-magnetic nanoparticles composite multifunctional scaffolds for bone tissue regeneration and hyperthermia treatment. International Journal of Bioprinting 10(6), 4538. https://doi.org/10.36922/ijb.4538

Nie, Y., Li, D., Peng, Y., Wang, S., Hu, S., Liu, M., Ding, J., and Zhou, W. (2020). Metal organic framework coated MnO2 nanosheets delivering doxorubicin and self-activated DNAzyme for chemo-gene combinatorial treatment of cancer. International Journal of Pharmaceutics 585, 119513. https://doi.org/10.1016/j.ijpharm.2020.119513

Zhong, D., Xie, W., Liao, Z., Liu, H., Zhu, L., Gao, F., Li, X., Yin, Z., Xu, G., Chen, P., Tian, J., Wang, L., Yin, K., Chen, K., and Wang, C. (2025). YTHDF1 transcriptionally activated by TCF4 suppresses osteoblast ferroptosis in titanium nanoparticle-induced osteolysis by accelerating GPX4 and SLC7A11 translation. Journal of Nanobiotechnology 23(1), 783. https://doi.org/10.1186/s12951-025-03861-6